

MAGNETISM

Qubit spin ice

Andrew D. King^{1*}, Cristiano Nisoli^{2*}, Edward D. Dahl^{1,3},
Gabriel Poulin-Lamarre¹, Alejandro Lopez-Bezanilla²

Artificial spin ices are frustrated spin systems that can be engineered, in which fine tuning of geometry and topology has allowed the design and characterization of exotic emergent phenomena at the constituent level. Here, we report a realization of spin ice in a lattice of superconducting qubits. Unlike conventional artificial spin ice, our system is disordered by both quantum and thermal fluctuations. The ground state is classically described by the ice rule, and we achieved control over a fragile degeneracy point, leading to a Coulomb phase. The ability to pin individual spins allows us to demonstrate Gauss's law for emergent effective monopoles in two dimensions. The demonstrated qubit control lays the groundwork for potential future study of topologically protected artificial quantum spin liquids.

Artificial spin ices are systems of interacting components characterized by frustrated binary variables whose collective behavior emerges from local constraints based on the two-in-two-out "ice rule" (Fig. 1A). They were initially introduced (1, 2) as analogs of the frustrated rare earth pyrochlores (3, 4) but then evolved to generate, through frustration and disorder, exotic emergent phenomena not found in natural systems (5). In simple ice-rule systems, the low-energy collective states can be described in terms of their excitations, which are emergent magnetic monopole quasiparticles (6–9). The most common artificial spin ice realizations have been based on lithographically patterned nanomagnets (10, 11). The more general set of ideas has been exported to other platforms, including colloids and superconducting vortices confined to bistable traps, and even to liquid crystals (12) and exotic mechanics of soft modes (13).

We implemented a two-dimensional (2D) spin ice of superconducting qubits—macroscopic quantum objects (14)—in a quantum annealing (QA) system and drove it between low-energy quasi-classical states by means of primarily quantum rather than thermal fluctuations, thus opening the door to future studies of quantum phases in these systems (15, 16). Our "qubit spin ice" does not require fixed prefabrication; instead, its energetic coupling terms can be fine tuned, and spins can be pinned at will. We exploited this flexibility to demonstrate how Gauss's law emerges from geometric constraints in two dimensions. By fixing the total flux of magnetization into the system's boundary, we injected topological charges into the ground state, demonstrating

induction of magnetic monopole quasiparticles that, unlike in dipolar implementations, interact purely entropically.

Square spin ice consists of a set of classical dipole spins placed along the edges of a square lattice (Fig. 1B). The spins impinging on vertices realize 16 different vertex configurations that are grouped by topology into Type I, ..., Type IV (Fig. 1A). The first two types obey the so-called "ice rule" (two spins point in, two point out) and are energetically favored in spin ice materials. The other two violate the ice rule, as signaled by their topological charge (defined as the difference between spins pointing in and out) of ± 2 and ± 4 , respectively, and are monopole excitations. Vertex energies are dictated by the antiferromagnetic couplings J_{\parallel}/J_{\perp} between spins impinging on the vertex collinearly and perpendicularly, respectively, and are $\epsilon_1 = -4J_{\perp} + 2J_{\parallel}$, $\epsilon_{II} = -2J_{\parallel}$, $\epsilon_{III} = 0$, and $\epsilon_{IV} = 4J_{\perp} + 2J_{\parallel}$. The resulting system is geometrically frustrated.

Before discussing the phases of this ice system, we describe the QA system with which we realized square ice in its well-known Ising form (15). The QA system comprises a set of superconducting flux qubits that interact through two-body couplers (17, 18), physically realizing the transverse-field Ising model generically described by the Hamiltonian

$$\mathcal{H} = \mathcal{J} \left(\sum_{\langle ij \rangle} J_{ij} \hat{\sigma}_i^z \hat{\sigma}_j^z + \sum_i h_i \hat{\sigma}_i^z \right) - \Gamma \sum_i \hat{\sigma}_i^x \quad (1)$$

where $\hat{\sigma}_i$ are Pauli matrices describing the qubit degrees of freedom, the tensor J_{ij} describes the action of the couplers, and h_i is a per-qubit longitudinal field. The terms J_{ij} and h_i can be programmed at will; local fields h_i are always set to zero except when specified.

Unlike in the Hamiltonians proposed to describe quantum spin ice in pyrochlores (19),

we have no quantum entanglement in the two-body coupling terms. Thus, in absence of the transverse field Γ , the ground state of \mathcal{H} is a set of Fock states that can be mapped into purely classical ones—namely, the Fock product of eigenvectors of the Pauli matrices $\hat{\sigma}^z$. However, switching on the transverse field entangles the binary quantum variables, subjecting them to quantum fluctuations.

At finite temperature, the QA system relaxes toward the thermal equilibrium of \mathcal{H} . Rapidly decreasing Γ and increasing \mathcal{J} projects this thermal distribution to the $\hat{\sigma}^z$ basis. This approach has recently been used for a variety of quantum Ising systems at finite temperature (20–22) and has provided the most direct observation of many-body quantum annealing dynamics to date (23).

To realize square ice in the QA system, we began with an Ising model (15): We consider an alternating A/B bipartition of vertices in the square lattice, calling a spin $S = 1$ (Fig. 1B, red) if it points toward an A vertex, or $S = -1$ (Fig. 1B, blue) if it points toward a B vertex. This gives an antiferromagnetic Ising model on a checkerboard lattice (Fig. 1C) whose quantum extension is captured by the Hamiltonian in Eq. 1. However, the geometry of qubit pairs that can be directly coupled is described by a "Chimera" graph (17, 18), which does not contain the required checkerboard lattice as a subgraph. We therefore represent each ice spin with a chain of four qubits, forced to act collectively with strong ferromagnetic couplings. These chains are intercoupled in a checkerboard geometry (Fig. 1D), whose tiling across the QA chip gives a 14 by 14 grid of ice vertices, with eight site vacancies resulting from inoperable qubits.

We calibrated the system to degeneracy (18) and used this point to define the nominal ratio $J_{\parallel}/J_{\perp} = 1$. The overall energy scale $J = J_{\parallel} = J_{\perp}$ is taken as the average total coupling between coupled four-qubit chains. J_{MAX} indicates the maximum achievable value of this Ising energy scale. The relationship between J_{\perp} and J_{\parallel} determines the relative energies of Type I and Type II vertices. Three cases are possible.

When $J_{\perp} = J_{\parallel} = J$, the six ice rule-obeying vertices (Type I and Type II) have the lowest energy, and the ground state is a degenerate manifold with residual entropy described by the degenerate six-vertex model (24). Its elementary excitations are monopoles (Type III), and the crossover temperature into the ice state is $T_{\text{ice}} \approx J$, or half the energy of a monopole.

When $J_{\perp} > J_{\parallel}$, the Type I vertices have the lowest energy, and their tiling forms a long-range ordered, classical ground state that is typical of the early antiferromagnetic artificial spin ice realizations (1, 25).

When $J_{\perp} < J_{\parallel}$, the Type II vertices have the lowest energy, and their tiling forms a

¹D-Wave Systems, Burnaby, British Columbia V5G 4M9, Canada. ²Theoretical Division, Los Alamos National Laboratory, Los Alamos, NM 87544, USA. ³Associate Laboratory Directorate for Simulation and Computation, Los Alamos National Laboratory, Los Alamos, NM 87544, USA.

*Corresponding author. Email: aking@dwavesys.com (A.D.K.); cristiano@lanl.gov (C.N.)

disordered ground state (“line state”) of subextensive entropy (8).

To probe equilibrium properties in these cases, we strobed the transverse field in a repeated relaxation protocol (23), starting from a randomly generated classical spin state. We simultaneously turned on both quantum ($\Gamma \approx J_{\text{MAX}}/3$) and thermal ($T = 10 \text{ mK} \approx J_{\text{MAX}}/12$) fluctuations for an exposure time of $256 \mu\text{s}$ then turned them off rapidly and read out a projected classical spin state. A single programming of the chip repeats this on/off cycle of fluctuations 128 times, producing a chain of 128 classical spin states; each is in or near the ground state manifold of the classical Ising Hamiltonian. We performed many repeated experiments with J ranging from $J_{\text{MAX}}/32$ to J_{MAX} . Classical spin states for the Ising model depicted in Fig. 1D were read from the QA then converted to states for the checkerboard Ising model (Fig. 1C), which in turn were converted to dipole configurations (Fig. 1B). An example is provided in fig. S7 (18).

The results of this measurement for the 14 by 14 ice system are shown in Fig. 2 at different energy scales J for the three cases $J_{\perp} = J_{\parallel}$, $J_{\perp} > J_{\parallel}$, and $J_{\perp} < J_{\parallel}$. The first column shows the relative frequency of vertex types throughout the lattice; the other columns show the spin structure factor, including pinch-point detail, computed from average spatial correlations (18). A larger coupling J leads to ensembles closer to the predicted ground states, with monopole excitations appearing only rarely. At the degeneracy point $J_{\parallel} = J_{\perp}$, the relative occurrences of Type I and Type II at high J very closely match those expected in the monopole-free degenerate ground state of spin ice, described by the six-vertex model (24). From the above, the coupling at the crossover to the ice manifold can be estimated to be $J_{\text{ice}} \approx J_{\text{MAX}}/12$, and thus, the data points $J/J_{\text{MAX}} = 1/16, 1/8$ sit near the crossover, where monopoles become sparse.

Minimal (2%) tuning of J_{\perp}/J_{\parallel} away from degeneracy leads to the relative promotion of Type I or Type II vertices, with an effect that increases with J . The strong sensitivity to degeneracy lifting is also apparent in the static spin structure factor $S(\mathbf{q})$. For weak coupling, bias toward Type I or Type II is barely perceptible. For strong coupling, we see at degeneracy the familiar, transverse structure—including the typical pinch-point singularities—associated with the Coulomb phase in an algebraic spin liquid (26). As the system is tilted toward Type I vertices, the structure factor becomes dominated by the Bragg peaks of the long-range Néel ordering. Likewise, tilting the system away from Type I vertices shows a line state of Type II vertices with long-range collinear spin-spin correlation.

We next concentrated on the degenerate case $J_{\perp} = J_{\parallel}$. Unlike in nanomagnetic realizations, longitudinal fields in qubit ice (Eq. 1, h_z)

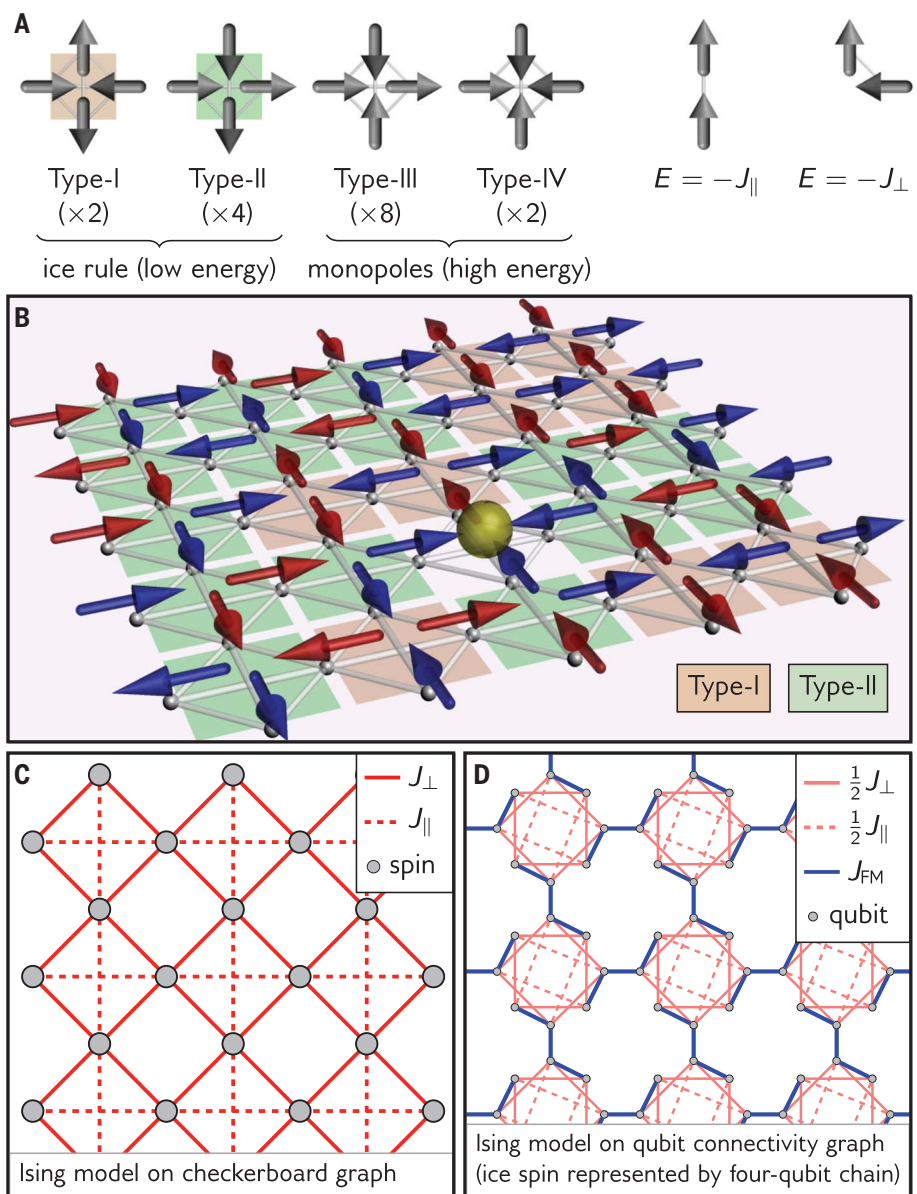


Fig. 1. Realizing square ice in a quantum annealer. (A) Each square ice vertex involves four dipoles that point in or out; 6 of 16 configurations satisfy the two-in-two-out ice rule. The remaining vertices have charge ± 2 (Type III) or ± 4 (Type IV) and host monopoles. Two coupling energies, J_{\parallel} and J_{\perp} , determine energetic preference between Type I and Type II vertices in the artificial spin ice. (B) Schematic of a square spin ice with dipoles colored according to their Ising representation (red = 1, blue = -1), with a monopole of net charge of +2 (yellow sphere). (C) Ising spin representation of (A). Ice vertices (squares with dotted diagonals) form corner-sharing plaquettes of four Ising spins (circles) each. (D) Embedding of (C) into the qubit connectivity graph (supplementary materials). To realize the checkerboard geometry, each spin in (C) is represented by using four qubits (circles), which are forced to act collectively through strong ferromagnetic coupling (blue lines). Two chains impinging on the same ice vertex are coupled by using two antiferromagnetic couplers, so each J_{\perp} or J_{\parallel} term is split into two equal coupling terms (red lines).

can act on individual qubits. We used these fields to pin a subset of spins and to demonstrate induction of a single, itinerant monopole, by Gauss’s law, as well as entropic interactions between monopoles.

We first pinned the boundary spins into a fixed antiferromagnetic boundary condition.

By Gauss’s law, the net flux of magnetization into the system is equal to the charge inside the system. Therefore, when we annealed the degenerate system under these boundary conditions, we typically found zero monopoles—a ground state. But if we flipped one fixed boundary spin, as shown in real-space in Fig. 3,

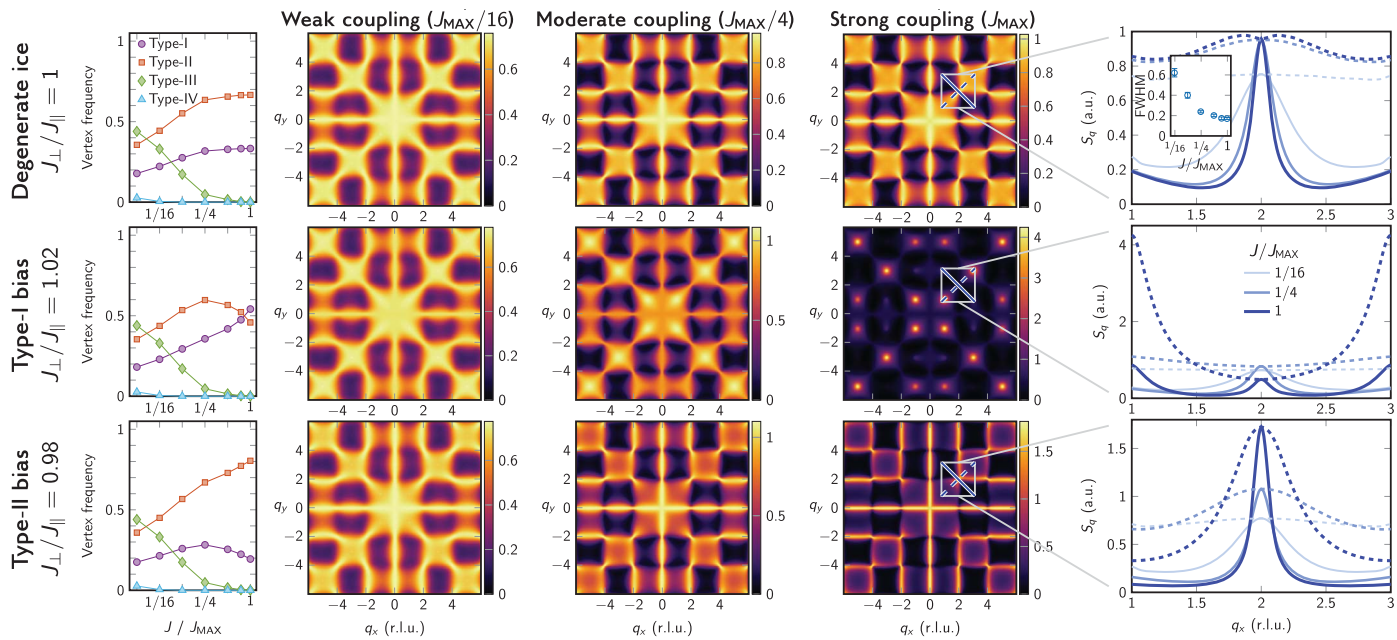


Fig. 2. Experimental results: fine-tuning the ice ensemble. The degenerate cases (top) $J_{\perp} = J_{\parallel}$, (middle) $J_{\perp} = 1.02J_{\parallel}$, and (bottom) $J_{\perp} = 0.98J_{\parallel}$. (Left) Frequencies of the different vertex types (Fig. 1A) versus the energy scale J/J_{MAX} , averaged over many measurements in a 14 by 14 ice system. (Middle left, middle, and middle right) Structure factor $S(\mathbf{q})$ (arbitrary intensity units) for varying coupling energy scale in the three cases, in reciprocal lattice space. (Right) Cross

sections of $S(\mathbf{q})$ at the pinch points. The degenerate case shows the pinch point singularity associated with the Coulomb phase. (Inset) The FWHM is the reciprocal correlation length, decaying as coupling energy increases (temperature is constant) and saturating in the strong coupling limit owing to finite system size. Tuning away from degeneracy results in the expected Bragg peaks (middle row) and collinear correlations (bottom row).

we forced a net flux, such as $=2$, into the system. Upon annealing, we then observed a net charge in the bulk, in the form of a free monopole of charge 2—in this case, the ground state contained a monopole by Gauss's law. Thus, an isolated monopole charge was induced in absence of a corresponding anticharge, by forcing a net flux on the boundaries. We must also pin the interior boundary spins produced by any vacancies caused by inoperable qubits.

We also observed a quantum-activated random walk of these monopoles. Thermal fluctuations have been used to drive spin dynamics in superparamagnetic nanoislands (27–29); in this work, the spin dynamics are driven by both quantum and thermal fluctuations (fig. S5) (18). Modifying the previous protocol (with $J_{\parallel} = J_{\perp} = J_{\text{MAX}}$), we strobed fluctuations for exposures of $1 \mu\text{s}$, the minimum interval permitted by the control circuitry.

For large Γ or long exposure, one expects that the quantum fluctuations would erase the system memory. However, for a carefully chosen value of $\Gamma = 0.34J_{\text{MAX}}$ for $1 \mu\text{s}$, the quantum-activated system preserves memory of its previous classical state, and the qubit kinetics, although activated primarily by quantum fluctuations, reveals monopole motion, monopole pair creation and annihilation, and collective flipping of closed loops of spins.

These phenomena are shown in Fig. 3 in a sequence of samples from a QA experiment.

In Fig. 3, we highlight the difference between successive QA states. These are suggestive of a random walk of a monopole, although we cannot rule out intermediate creation and annihilation of additional monopole pairs. Most samples contain only the isolated monopole induced into the ground state by means of a nonzero-flux boundary condition, but after 70 exposures to fluctuations, a surplus monopole pair appears, making the ensuing sequence particularly interesting to visualize. After 70 exposures, there are three monopoles for an overall net charge +2, which matches the boundary flux. At time (t) = $71 \mu\text{s}$, two monopoles of opposite charge have mutually annihilated, returning the system to the ground state. At $t = 72 \mu\text{s}$, the induced monopole has moved again, and by $t = 77 \mu\text{s}$, several steps later, it has traversed much of the available space. These time scales are in sharp contrast to the multisecond relaxation observations in nanoisland and colloidal implementations (9, 28, 30). Example state sequences are shown in movies S1 to S6 (18).

Unlike in fully dipolar spin ice (6), our monopoles cannot interact directly because no appreciable long-range dipolar interaction exists between the qubits. Monopoles, however, can be thought of as emergent quasiparticles in an underlying spin structure and are therefore correlated by the divergence-free spin vacuum. This correlation can be described as a pairwise interaction by which oppositely charged par-

ticles attract, but the attraction is merely a result of the degeneracy of spin configurations that are compatible with the monopole positions: It is an entropic interaction, and its coupling constant depends on temperature (31). In this 2D system, it corresponds to the 2D Coulomb law between charges q_1 and q_2 at distance x , which is logarithmic $\sim q_1 q_2 T \ln(x)$, and thus leads to a Bessel screening, or $\langle q(x) \rangle \propto K_0(x/\xi)$, where K_0 is the modified Bessel function and ξ is a temperature-dependent correlation length (31).

We can probe this purely entropic screening between monopoles by pinning a monopole at the center of our geometry. The result of this pinning is shown in Fig. 4, which compares it to the boundary conditions described above. With open boundaries or with zero net flux (Fig. 4, A and B), monopoles are absent in the ground state and therefore are only rarely observed after annealing. With a net flux of 2 (as in Fig. 3), by Gauss's law a monopole is forced into the system's ground state. Simulating the system repeatedly with random assignments of the flipped boundary spin, we found that the probability of finding a monopole is fairly flat across the lattice (Fig. 4C). Thus, when flux inside the system is fixed, the forced monopole is delocalized in the bulk, as one would expect. By contrast, when a monopole is pinned at the center and boundaries enclose zero flux (Fig. 4D), we observed a second, free monopole in

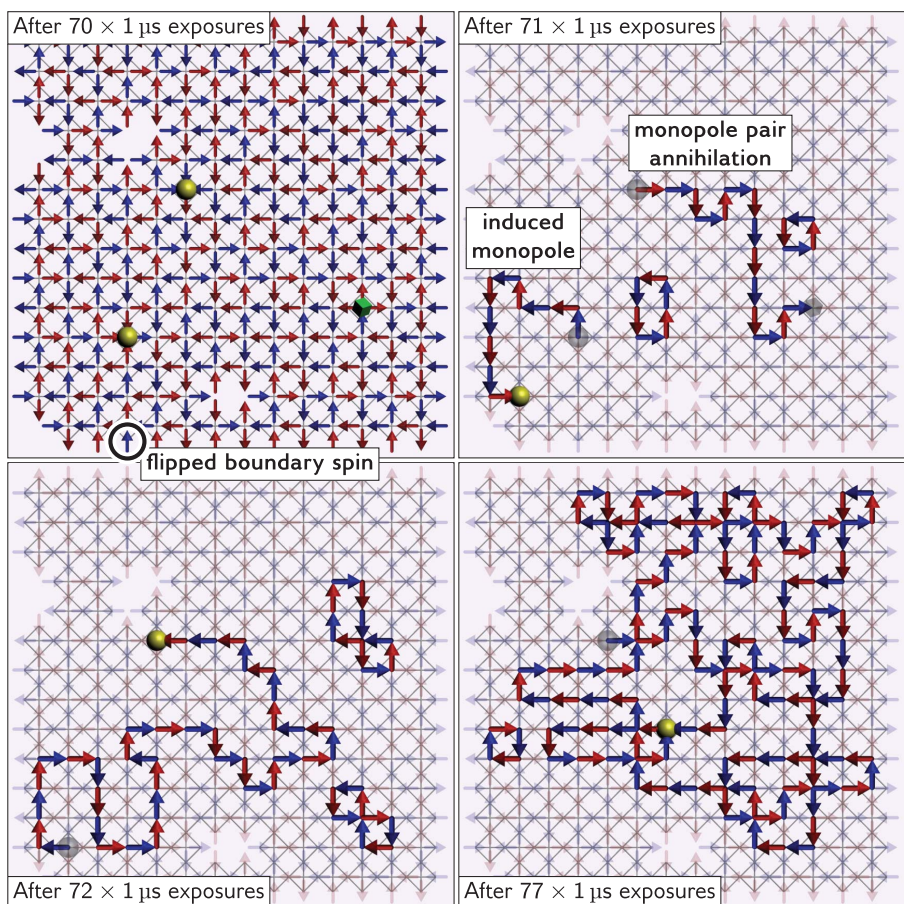


Fig. 3. Gauss's law and monopole kinetics. Successive QA samples with monopoles (positive ones are indicated with a yellow sphere, negative ones with a green cube). Boundary spins (including defect boundaries) can be clamped by using per-qubit longitudinal fields. Forcing antiferromagnetic alignment of boundary spins gives no net flux of magnetization in the system; flipping a single boundary spin (shown) gives a net flux of 2 and thus induces a monopole in the ground state. The difference between two successive QA samples (faded arrows are unchanged from the previous spin state) shows the net motion of an induced monopole. In this example, we also see annihilation of two monopoles and small regions of local reconfiguration. Missing spins indicate vacancies as described in the text.

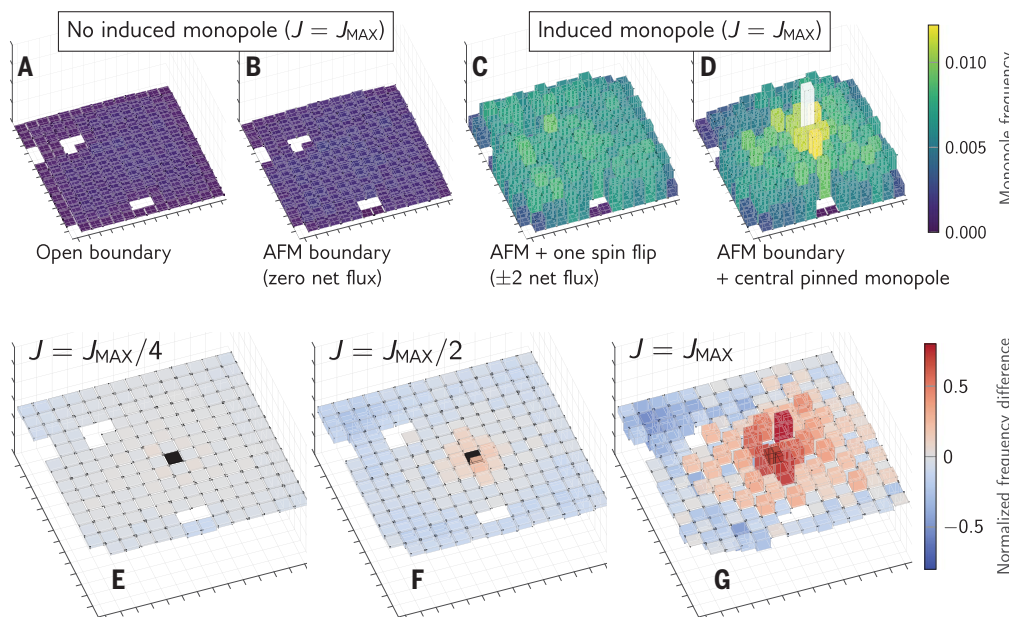


Fig. 4. Monopole frequency and interaction. (A to D) Four boundary conditions. (A) Open boundary conditions. (B) Zero boundary flux, where boundary spins are forced to align antiferromagnetically (AFM). (C) Nonzero net flux, where a random boundary spin is flipped from the AFM background. (D) AFM boundaries with a central pinned monopole, where a central vertex is forced into a Type III configuration. Structural vacancies in the lattice are shown as missing data; in (D), the pinned monopole is indicated with a white bar.

(E to G) Using state (C) as a background density for an induced monopole, we take the difference between (D) and (C), normalized by the average frequency in (C), to demonstrate monopole-monopole entropic interaction. (H) Entropic screening of charge shows good agreement with a Bessel decay form for weak coupling. For strong coupling, the correlation length is large compared with finite system size, leading to a poor fit. Data and error bars indicate the mean, maximum, and minimum values for a given Euclidean distance.

the bulk that cancels the net charge of the pinned monopole. At high coupling, the probability of finding a free monopole was maximal close to the pinned one. We also observed evidence of an alternating decay pattern that depends on the parity of the grid distance (ℓ_1 norm) between two vertices (31). This phenomenon was more visible in absence of site vacancies (fig. S6) (18).

At lower coupling, more monopoles were available to screen the pinned charge, and the relative influence on monopole population was smaller (Fig. 4, E to G). In Fig. 4H, we plot average vertex charge, over many sampled states, as a function of lattice distance from the pinned monopole, revealing charge screening: For weak coupling, screening is highly localized and in good agreement with the theoretically expected $K_0(x/\xi)$ Bessel decay form. The correlation length is known to be infinite in the ground state and thus grows with coupling. For strong coupling, the correlation length is comparable with system size [Fig. 2, inset, plot of full width at half maximum (FWHM)], and the screening becomes flatter.

Last, in a square spin ice, the only kinetics that does not require an activation energy proceeds either through monopole motion or the much less likely collective flipping of entire loops of spins. Not surprisingly, we found that forcing itinerant monopoles into the sample, either with Gauss's law or pinned monopoles, leads to faster equilibration (fig. S5) (18) because the extra charge acts as a mobile catalyst for mixing.

The reconfigurability of our system will enable its generalization to a variety of lattice geometries (32), including Kagome and 3D pyrochlore lattices (33) in near-term QA systems. Despite evidence for a quantum-driven local dynamics, the observation of a macroscopic quantum phase (15, 16) remains out of

reach at the operating temperature in this simulation (18); however, these experiments offer vistas toward engineering a quantum spin liquid (15, 16, 19, 34). Future quantum annealers will allow logical spins with greater low-temperature tunneling, expanding the study of collective quantum phenomena in frustrated systems.

REFERENCES AND NOTES

- R. F. Wang *et al.*, *Nature* **439**, 303–306 (2006).
- M. Tanaka, E. Saitoh, H. Miyajima, T. Yamaoka, Y. Iye, *Phys. Rev. B Condens. Matter Mater. Phys.* **73**, 052411 (2006).
- A. P. Ramirez, A. Hayashi, R. J. Cava, R. Siddharthan, B. S. Shastry, *Nature* **399**, 333–335 (1999).
- S. T. Bramwell, M. J. Gingras, *Science* **294**, 1495–1501 (2001).
- C. Nisoli, V. Kapaklis, P. Schiffer, *Nat. Phys.* **13**, 200–203 (2017).
- C. Castelnovo, R. Moessner, S. L. Sondhi, *Nature* **451**, 42–45 (2008).
- I. Ryzhkin, *J. Exp. Theor. Phys.* **101**, 481–486 (2005).
- Y. Perrin, B. Canals, N. Rougemaille, *Nature* **540**, 410–413 (2016).
- A. Farhan *et al.*, *Sci. Adv.* **5**, eaav6380 (2019).
- C. Nisoli, R. Moessner, P. Schiffer, *Rev. Mod. Phys.* **85**, 1473–1490 (2013).
- S. H. Skjærø, C. H. Marrows, R. L. Stamps, L. J. Heyderman, *Nat. Rev. Phys.* **2**, 13–28 (2019).
- A. Ortiz-Ambriz, C. Nisoli, C. Reichhardt, C. J. Reichhardt, P. Tierno, *Rev. Mod. Phys.* **91**, 041003 (2019).
- A. S. Meeussen, E. C. Oğuz, Y. Shokef, M. van Hecke, *Nat. Phys.* **16**, 307–311 (2020).
- R. Harris *et al.*, *Phys. Rev. B* **81**, 1 (2010).
- L.-P. Henry, T. Roscilde, *Phys. Rev. Lett.* **113**, 027204 (2014).
- C. Chamon, D. Green, Z.-C. Yang, *Phys. Rev. Lett.* **125**, 067203 (2020).
- P. I. Bunyk *et al.*, *IEEE Trans. Appl. Supercond.* **24**, 1–10 (2014).
- Materials and methods are available as supplementary materials.
- M. J. Gingras, P. A. McClarty, *Rep. Prog. Phys.* **77**, 056501 (2014).
- R. Harris *et al.*, *Science* **361**, 162–165 (2018).
- A. D. King *et al.*, *Nature* **560**, 456–460 (2018).
- P. Weinberg *et al.*, *Phys. Rev. Lett.* **124**, 090502 (2020).
- A. D. King *et al.*, *Nat. Commun.* **12**, 1113 (2021).
- E. H. Lieb, *Phys. Rev.* **162**, 162–172 (1967).
- J. P. Morgan, A. Stein, S. Langridge, C. H. Marrows, *Nat. Phys.* **7**, 75–79 (2011).
- C. L. Henley, *Annu. Rev. Condens. Matter Phys.* **1**, 179–210 (2010).
- J. M. Porro, A. Bedoya-Pinto, A. Berger, P. Vavassori, *New J. Phys.* **15**, 055012 (2013).
- A. Farhan *et al.*, *Phys. Rev. Lett.* **111**, 057204 (2013).
- V. Kapaklis *et al.*, *Nat. Nanotechnol.* **9**, 514–519 (2014).
- A. Ortiz-Ambriz, P. Tierno, *Nat. Commun.* **7**, 10575 (2016).
- C. Nisoli, *Phys. Rev. B* **102**, 220401 (2020).
- M. J. Morrison, T. R. Nelson, C. Nisoli, *New J. Phys.* **15**, 045009 (2013).
- G.-W. Chern, C. Reichhardt, C. Nisoli, *Appl. Phys. Lett.* **104**, 013101 (2014).
- M. Stern, C. Castelnovo, R. Moessner, V. Oganesyan, S. Gopalakrishnan, Quantum percolation of monopole paths and the response of quantum spin ice. arXiv:1911.05742 [cond-mat.stat-mech] (2019).
- A. D. King, C. Nisoli, E. D. Dahl, G. Poulin-Lamarre, A. Lopez-Bezanilla, Qubit spin ice. Zenodo (2021); doi:10.5281/zenodo.4776361.

ACKNOWLEDGMENTS

We acknowledge the contributions of the processor development and fabrication teams at D-Wave, without whom this work would not be possible. A.D.K. thanks A. Banerjee (Purdue) and C.N. thanks P. Schiffer (Yale), A. Bishop (LANL), and N. Rougemaille (Institut Néel) for in-depth discussions. **Funding:** The work of A.L.-B., E.D.D., and C.N. was carried out under the auspices of the US Department of Energy (DOE) through the Los Alamos National Laboratory, operated by Triad National Security (contract 892333218NCA000001). We thank ISTI at Los Alamos National Laboratory for financial support; work was also supported by the Institute for Materials Science (IMS) at Los Alamos under the program of “IMS Rapid Response.” C.N. work was supported by a DOE LDRD grant. The work of A.D.K., E.D.D., and G.P.-L. was funded by D-Wave. **Author contributions:** A.L.-B., E.D.D., and C.N. conceived the project. C.N., A.D.K., A.L.-B., and E.D.D. contributed to experimental design. E.D.D. realized the embedding. A.D.K. performed the QA experiments and data analysis. G.P.-L. calibrated the QA processor and performed supporting measurements. C.N. performed theoretical analysis and drafted the manuscript with A.D.K. All authors contributed to the final version of the manuscript. **Competing interests:** A.D.K., E.D.D., and G.P.-L. are current or recent employees of and/or holders of stock options in D-Wave, which designs, manufactures, and sells the QA apparatus used in this work, and declare a competing interest on that basis. C.N. and A.L.-B. declare no competing interests. **Data and materials availability:** Experimental data are available online (35).

SUPPLEMENTARY MATERIALS

- science.sciencemag.org/content/373/5766/suppl/DC1
 Materials and Methods
 Supplementary Text
 Figs. S1 to S7
 References (36, 37)
 Movies S1 to S6
- 11 August 2020; accepted 17 June 2021
 Published online 15 July 2021
 10.1126/science.abe2824

Qubit spin ice

Andrew D. KingCristiano NisoliEdward D. DahlGabriel Poulin-LamarreAlejandro Lopez-Bezanilla

Science, 373 (6554), • DOI: 10.1126/science.abe2824

A reconfigurable spin ice

Spin ices, magnetic systems in which local spins respect the so-called ice rules, can occur in natural materials or be engineered in patterned arrays. King *et al.* used superconducting qubits to implement a two-dimensional artificial spin ice. By changing the strength and ratio of spin couplings, the researchers were able to access a variety of ground states. Arranging the boundary spins in an antiferromagnetic configuration and then flipping one of those spins generated a magnetic monopole in the system's interior. —JS

View the article online

<https://www.science.org/doi/10.1126/science.abe2824>

Permissions

<https://www.science.org/help/reprints-and-permissions>